Astron. Astrophys. 332, 686–694 (1998)

ASTRONOMY
AND
ASTROPHYSICS

A re-evaluation of profile shapes from resonance line scattering in spherical stellar winds

R. Ignace

Department of Physics and Astronomy, University of Glasgow, Glasgow, G12 8QQ, UK

Received 14 July 1997 / Accepted 23 December 1997

Abstract. It is common to treat the scattering of light by resonance lines as isotropic, but in fact it has been known for some time that general resonance line scattering is partially isotropic and partially dipolar, the relative strength of the two components depending on the specific transition. As a result, the profile shapes of lines that scatter with strong dipole distributions could in principle differ markedly from those that scatter isotropically. This paper explores the consequences of general resonance line scattering in spherically symmetric stellar envelopes. As a simplified example, a resonance line profile arising in a constant expansion wind is shown *not* to be flat-top in shape, as commonly accepted, but can in fact exhibit a symmetric *double-horned* shape. Although interesting, the case of constant expansion has limited application. Using the Sobolev-P method, sample line profiles are computed for a typical wind velocity distribution that is often assumed in hot star winds. These simulated lines reveal that anisotropic scattering yields profile shapes that are centrally depressed and broadened. Taking account of finite star effects, the emission profile of an optically thin resonant line that is purely Rayleigh scattering (like a free electron) differs from that of the isotropic scattering case at only the 10% level, and the two types of profiles become indistiguishable for increasing line optical depths owing to the effects of multiple scattering. Relative to the case of isotropic scattering, the anisotropic scattering has little effect in altering the emission profile shape, a consequence of (a) stellar occultation and (b) finite star depolarization. Thus, except for the case of a shell of considerable radius, the accuracy of resonance line profile computations in *spherically symmetric* extended envelopes are hardly compromised by the effects of anisotropic scattering.

Key words: line: formation – line: profiles – techniques: spectroscopic – stars: circumstellar matter – stars: early-type – stars: mass-loss

1. Introduction

As resonance lines are typically the strongest observed spectral features from hot star winds, especially at the UV wavelengths, and are of importance for diagnosing the wind properties (Friend & Abbott 1986; Pauldrach et al. 1986; Kudritzki & Hummer 1990) this paper concerns the generalization of profile shapes expected from anisotropic resonance line scattering in spherical winds. Several authors have considered the polarized radiative transfer of resonance lines in stellar atmospheres (Nagendra 1988; McKenna 1984, 1985) and in stellar winds (Caroff et al. 1972; Jeffery 1989, 1990), but a discussion of the case considered here and the resulting profiles was not given in those works.

For resonance line scattering, the emission process is not in general purely isotropic (Hamilton 1947), but consists of mixed isotropic and dipole contributions. In the theory of line formation in stellar winds, it is a well-known result that an optically thin wind line formed in a constant expanding spherical wind will have a "flat-topped" profile shape. This conclusion holds for both recombination and resonance lines. However, the flat-top profile result assumes that (a) stellar occultation may be ignored and (b) the line emission is isotropic. Thus, the flat-top shape is not a general result for anisotropically scattering resonance lines, even if stellar occultation can be ignored. One can also expect modifications to the emission profile shape formed in winds with more realistic velocity distributions. Consideration of anisotropic scattering in the spherical case is especially worth pursuing because although the symmetry ensures that the net polarization from an unresolved circumstellar envelope is zero, the anisotropic scattering is still of consequence for the observed profile shape.

Instead of immediately launching into the computational aspects of the line profile generation, it is useful first to briefly review how resonant scattering can give rise to polarized emission. Recall that a resonant transition involves the absorption of a photon that excites an electron in lower level l to an upper level u and then subsequently decays back to level l, so that "emission" here is referred to as scattering, because the process conserves the stellar photon number. The polarimetric properties of the resonance line scattering arise as follows. Adopting the notation of Chandrasekhar (1960), the fraction of the resonance line scattering which is dipolar is given by the parameter E_1, that ranges in value from 0 to 1. The fraction of the scattering that is isotropic is just $1 - E_1$. The calculation of E_1 depends on the quantum number j_l of the lower level and the Δj of the permitted transition (see Table II of Chandrasekhar).

Send offprint requests to: rico@astro.gla.ac.uk

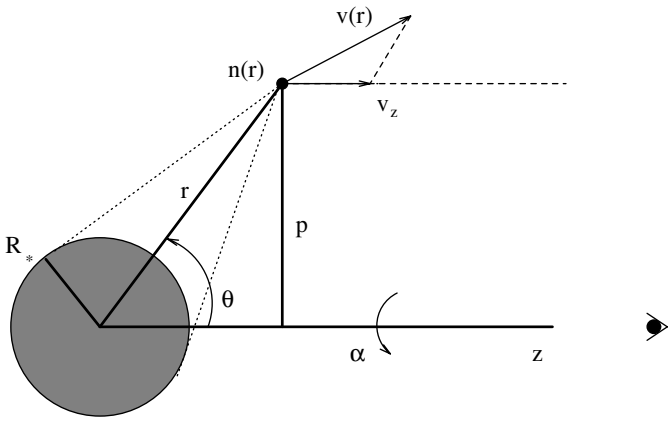

Fig. 1. Resonance line scattering in a circumstellar envelope of arbitrary density distribution $n(\mathbf{r})$ and velocity field $\mathbf{v}(\mathbf{r})$. The coordinates (p, α, z) and (r, θ) are the cylindrical and spherical coordinates of the observer and star, respectively. The variable $v_{\rm z}$ is the observed projected Doppler shift

Hamilton (1947) offers a simple explanation for the mixing of dipole and isotropic contributions in the resonance line scattering. For a line transition with $j_l = 0$ and $\Delta j = 1$, the bound electron is excited to a state that is analogous to a free electron, so the line scattering of light is dipolar, or Rayleigh scattering. However, unlike the free electron, which can be excited only in directions orthogonal to the propagation of the incident light, an atom can obtain a state of excitation that is classically given by dipole components in three orthogonal directions. For example, the transition with $j_l = 1$ and $\Delta j = -1$ corresponds to emission from a state ($j_{\rm u} = 0$) that is spherically symmetric (impossible for a free electron), hence the incident light for this case is scattered isotropically, as there is no preferred direction.

For stellar winds the consequences of the anisotropic scattering of light for resonance lines is that the observed intensity of line emission will depend on the scattering geometry (e.g., forward scattering versus that through a right angle). In a stellar wind, the scattered light will appear at a Doppler shifted frequency in the wind broadened profile that depends on the observed projected motions of the scatterers, hence there is a geometric relation common to both the line scattering and the Doppler shift at which the scattered light is observed. Concentrating on constant spherical expansion and assuming a stellar source of unpolarized light, forward and backward scattering occurs along the ray intercepting the center of the star, and the observed intensity of scattered light will be unpolarized. The forward and backward scattered light would appear in the extreme line wings, for the scatterers are maximally red and blue Doppler shifted with respect to the line-of-sight. In contrast, light appearing at line center arises from the plane of the sky where the velocity of expansion is perpendicular to the line-of-sight. In this case the scattering of light occurs through a right angle. For isotropic scattering, the amount of scattered light through a right angle is the same as for forward and backward scattering. However, this is not the case for dipole scattering, for which a smaller fraction of the incident light is scattered through a right angle than is forward or backward scattered. Hence, resonance lines that scatter with a strong dipole contribution are expected to have a double-horned shape in contrast to the simple flat-top that results from isotropic scattering. These kinds of considerations are developed further in this paper to explore the effects of general resonance line scattering for emission profiles from stellar winds.

In Sect. 2 the emission profile shapes are computed, first in the case of an optically thin constant expansion wind as discussed above and second in the case of a more realistic wind velocity distribution. The constant expansion case is useful for exploring the finite star effects, which for an optically thin wind yields insightful analytic solutions for the emission profile shape. In the case of velocity stratification, the Sobolev-P method of Jeffery (1990) is employed. A discussion of the results of the profile calculations for observations of spherical stellar winds is given in Sect. 3.

2. Resonance line scattering in spherical stellar winds

2.1. Optically thin profiles from a constant expansion spherical shell

There are advantages to considering the optically thin case first, and chief among them is that an analytic expression can be derived for the emission line profiles. Although of limited direct application, a study of analytic optically thin solutions permits a more direct grasp of the major effects of anisotropic scattering for the stellar wind line profiles. Consider the scattering of stellar light at a point $\mathbf{r}$ in an extended circumstellar envelope with number density of scatterers $n(\mathbf{r})$ and velocity field $\mathbf{v}(\mathbf{r})$ as shown in Fig. 1. Employing the Sobolev approximation (e.g., see Mihalas 1978), the stellar light interacts with atoms in an iso-velocity zone and with scattering cross-section

$$\sigma_\nu = \sigma_l \, \delta(\nu - \nu_{\rm z}). \tag{1}$$

The parameter σ_l is the frequency integrated cross section and is given by $\sigma_l = \lambda_{\rm ul}^2 g_{\rm u} A_{\rm ul}/8\pi g_l$, where $\lambda_{\rm ul}$ is the line wavelength, $A_{\rm ul}$ is the Einstein transition probability, and $g_{\rm u}$ and g_l are the statistical weights of the upper and lower levels. The δ-function ensures that the stellar light interacts with the scattering atoms only at a certain locus of points in the envelope. This locus of points is where the observed frequency ν is equal to the Doppler shifted frequency $\nu_{\rm z}$ of the scatterers along the line-of-sight, as given by

$$\nu_{\rm z} = \nu_{\rm ul} \left(1 + \frac{\mathbf{v} \cdot \hat{\mathbf{z}}}{c}\right). \tag{2}$$

The unit vector $\hat{\mathbf{z}}$ is in the direction of the observer.

It is convenient here to define the observed velocity Doppler shift as $v_{\rm z} = -\mathbf{v} \cdot \hat{\mathbf{z}}$. Then for optically thin resonance scattering, the observed flux of scattered light at Doppler shift $v_{\rm z}$ is given by

$$F_\nu(v_{\rm z}) \; = \; \frac{1}{D^2} \int_{v_{\rm z}} n(\mathbf{r}) \, \sigma_l \, \delta(\nu - \nu_{\rm z})$$

$$\left[J_\nu - \frac{1}{8} E_1 (3K_\nu - J_\nu)(1 - 3\cos^2\vartheta)\right] p dp d\alpha dz, \tag{3}$$

where the cylindrical coordinates (p, α, z) and the spherical coordinates (r, ϑ, α) are defined in Fig. 1, J_ν and K_ν are the familiar Eddington moments of the stellar radiation field that is assumed to emerge from a star of constant surface brightness, D is the distance to the star, and the Doppler shifted frequency $\nu_z = \nu_{ul}(1 - v_z/c)$. The terms appearing in the brackets inside the integral result from considerations of Rayleigh (i.e., dipole) scattering of the stellar intensity (see Chandrasekhar 1960; Stenflo 1994).

Eq. (3) concerns the emission profile only and does not include the effects of absorption. Naturally, the wind absorption dramatically influences the blueshifted profile shape, but not the redshifted emission (although near line center contamination from any photospheric contribution must be of concern). So, the discussion of anisotropic scattering effects emphasises the red wing emission to avoid the additional complexity presented by blueshifted absorption trough. It is further assumed that the wind is optically thin in the continuum. Using Eq. (3), emission profiles are derived for four cases: (a) point star, (b) occultation, (c) finite star depolarization effects, and (d) the combined results of (b) and (c). In all of these four cases, a constant expansion spherical wind is assumed with speed v_0.

In the spherically symmetric case, the viewing inclination is arbitrary, as there exists no preferred stellar axis, hence the stellar axis is taken as coincident with the z-axis of the observer. For constant expansion the iso-velocity zones of a geometrically thin spherical shell are rings of opening angle ϑ with Doppler shift $v_z = -v_0 \cos\vartheta$. For a radially extended wind expanding at v_0, the iso-velocity zones grow to become cones of opening angle ϑ.

2.1.1. The point star approximation

Treating the star as a point source of illumination for which $J_\nu = K_\nu = L_\nu/16\pi^2 r^2$, Eq. (3) for the flux in the line profile as a function of Doppler shift reduces to

$$F_\nu(v_z) = \frac{L_\nu}{16\pi^2 D^2}\,\sigma_l \int_{v_z} n(r)\,\delta(\nu - \nu_z) \left[1 - \frac{1}{4} E_1 (1 - 3\cos^2\vartheta)\right] 2\pi dr \sin\vartheta\, d\vartheta. \tag{4}$$

where the differential volume element $2\pi r^2\, dr \sin\vartheta\, d\vartheta$ was substituted for $2\pi p\, dp\, dz$. The wind number density of scatterers is taken as $n(r) = n_0 R_*^2/r^2$, where for the point star case R_* is taken as the innermost radius of the scattering volume and n_0 is the number density at $r = R_*$. Integrating over radius from R_* to ∞ and employing the following property of δ-functions,

$$\int_{-\infty}^{\infty} \delta\left[\nu - \nu_z(\vartheta)\right] d\vartheta = \left|\frac{d\nu_z}{d\vartheta}\right|^{-1} = \frac{\lambda_{ul}}{v_0 \sin\vartheta}, \tag{5}$$

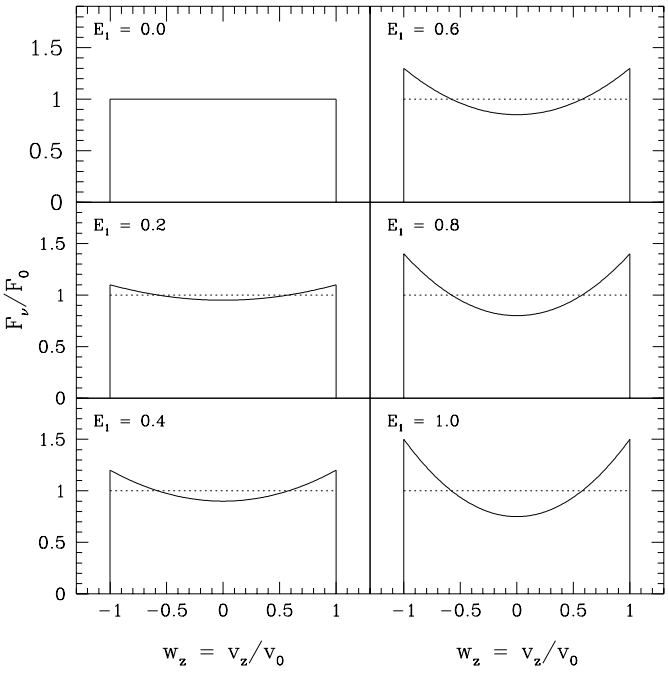

Fig. 2. Resonance scattering line profiles for a spherical wind and six values of the E_1 parameter treating the star as a point source of illumination. The dotted line is a reproduction of the flat-top result from the upper left panel

the flux from the spherical wind simplifies to

$$F_\nu(v_z/v_0 = \cos\vartheta) = \frac{L_\nu\,\sigma_l\,R_*\,n_0\,\lambda_{ul}}{8\pi\,v_0\,D^2} \left[1 - \frac{1}{4}\,E_1\,(1 - 3\,\cos^2\vartheta)\right]. \tag{6}$$

As expected for isotropic scattering with $E_1 = 0$, the line flux as a function of v_z is constant, and the profile is flat-topped. But for $E_1 \neq 0$, the line flux is a function of ϑ which relates to v_z, and the profile is therefore not flat-topped in this case.

For convenience let $F_0 = L_\nu\,\sigma_l\,R_*\,n_0\,\lambda_{ul}/8\pi\,v_0\,D^2$ and $w_z = v_z/v_0 = -\cos\vartheta$, then the normalized line profile flux becomes

$$\frac{F_\nu(w_z)}{F_0} = 1 - \frac{1}{4}\,E_1(1 - 3w_z^2). \tag{7}$$

The line profiles from this expression are plotted in Fig. 2 for values of E_1 = 0.0, 0.2, 0.4, 0.6, 0.8, and 1.0. The abscissa is the observed velocity shift w_z. The ordinate is the normalized line profile emission. For the cases of $E_1 \neq 0$, the flat-top profile that results for isotropic scattering is shown as a dotted line for comparison. In the case of $E_1 = 1$, the profile is strongly double-horned, but even with $E_1 = 0.4$, the profile shows deviations at the 20% level relative to the flat-top.

Double-horned line profiles with shapes like that of the $E_1 = 1$ case appear similar to what might be expected from an equatorial disk structure (e.g., profiles from rotating disks as in Struve [1931]). However, the profile shapes of Fig. 2 are

only valid if the star may be approximated as a point source. The results of this section also require that the flow be coasting at a constant speed. Although interesting, the only direct application of Eq. (7) is to scattering shells of large radius. The following derivations show that consideration of a star's finite size drastically modifies the emission line profile shape.

2.1.2. The effect of occultation

If the scattering region extends down to the stellar radius, then occultation cannot be ignored. The lower boundary to the integration over radius in Eq. (4) is now a function of the Doppler shift in the profile. With occultation, v_z gives the maximal *observed* receding velocity of a spherical shell of a radius $r = R$, such that $v_z = -v(R)\cos\vartheta(R) = -v(R)\sqrt{1 - R_*^2/R^2}$. Thus R represents the locus of points of intersection (being a circle) between the sphere of radius R, which varies with v_z in the line, and the occultation tube of cylindrical radius R_*. The velocity shift v_z is then the projection of $v(r)$ onto that occulting tube.

Assuming again that the wind expands at a constant speed, the lower boundary to the flux integral (4) reduces to $R(v_z) = R_*/\sqrt{1 - v_z/v_0} = R_*/\sin\vartheta$, and the integral solution becomes

$$\frac{F_\nu(w_z)}{F_0} = \left[1 - \frac{1}{4}\,E_1\,(1 - 3\,w_z^2)\right]\sqrt{1 - w_z^2}. \qquad (8)$$

This last expression applies only to the redshifted wing (i.e., $w_z \geq 0$, $\vartheta \in [\pi/2, \pi]$), because the blueshifted emission does not suffer from the stellar occultation. The appearance of the $\sin\vartheta$ factor has the correct limiting properties that (a) at $v_z = 0$, $\vartheta = \pi/2$, and there is no occultation effect and (b) at $v_z = v_0$, $\vartheta = \pi$, and the occultation is complete so that F_ν tends toward zero.

Fig. 3 demonstrates the effect of occultation on the red wing. The solid lines are the profiles from Fig. 2, and the dotted line shows the profile shape after accounting for stellar occultation. Clearly, the the redshifted horn is completely eliminated by the occultation. Yet, the figure suggests that for scattering regions extending to the stellar radius R_*, the profile shape should never be flat-topped for lines with $E_1 = 0$. Interestingly, now the major consequence for the anisotropic scattering is to make the red wing appear somewhat more rectangular.

Although some semblance of a flat-topped profile is actually recovered with increasing values of E_1, the overall height of the profile is reduced, so that the half equivalent width (the line equivalent width for $v_z \geq 0$) is very nearly constant. However, the line shape is quite different. In the following section, occultation is ignored, and emphasis is given to a second major effect of a star's finite size, namely the isotropizing effects of the incident stellar radiation field for scatterers located close to the stellar photosphere.

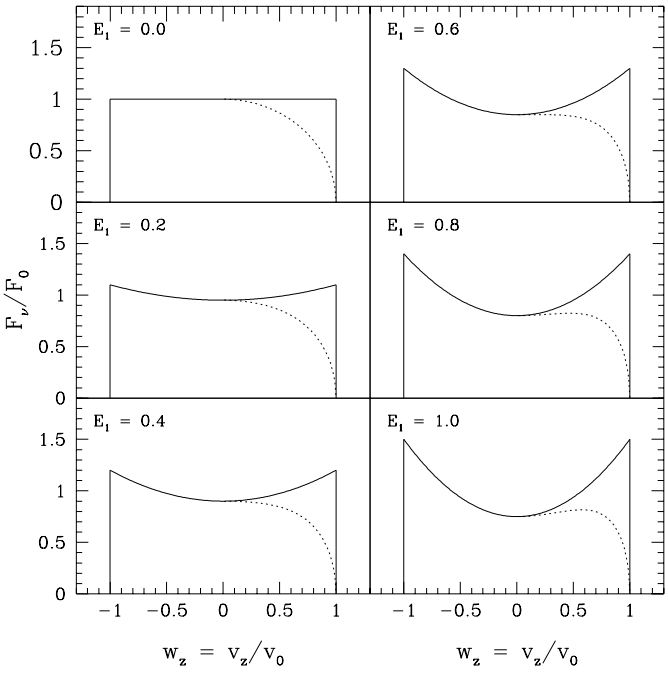

Fig. 3. Resonance scattering line profiles showing the effects of stellar occultation. Solid is for point source illumination, and dotted is for profiles with occultation

2.1.3. The effect of finite star depolarization

The finite stellar disk can alter the degree of anisotropic scattering in the inner wind owing to the more nearly isotropic incidence of the stellar radiation field at such locations (Cassinelli et al. 1987). In Eq. (4) for the point star case, the anisotropic scattering arises from the term $(1 - 3\cos^2\vartheta)$. For a point star, the observed light scatters through a single fixed value of ϑ between the observer's line-of-sight to the scatterer and the line connecting the star and the scatter. But in the case of a finite star, the intensity beams at the scatterer span a finite solid angle as subtended by the star at the scatterer's position. Thus, different beams are scattered through different angles (recalling that the observer is at a fixed position) with the net result that the scattered light is more isotropized relative to what emerges in the case of scattering from a point source. Naturally, at large distances, the star does approach that of a point source.

The observed flux of emission in the profile is found by returning to Eq. (3) with $J_\nu = \frac{1}{2}(1 - \cos\vartheta_*)I_\nu^*$ and $K_\nu = \frac{1}{6}(1 - \cos^3\vartheta_*)I_\nu^*$, where the geometrical factor $\cos\vartheta_* = \sqrt{1 - R_*/r}$ and $I_\nu^* = L_\nu/4\pi^2R_*^2$. Ignoring occultation the solution to the integral expression (3) is

$$\frac{F_\nu(w_z)}{F_0} = (\pi - 2)\,\left[1 - \frac{\pi/16}{\pi - 2}\,E_1\,(1 - 3\,w_z^2)\right]. \qquad (9)$$

There are two main differences between the case of finite star depolarization (9) as contrasted with the point star solution of Eq. (4), which are apparent from the profiles shown in Fig. 4. The first difference is that the numerical coefficient of the E_1 term is reduced from 0.25 in the point star case to just 0.172

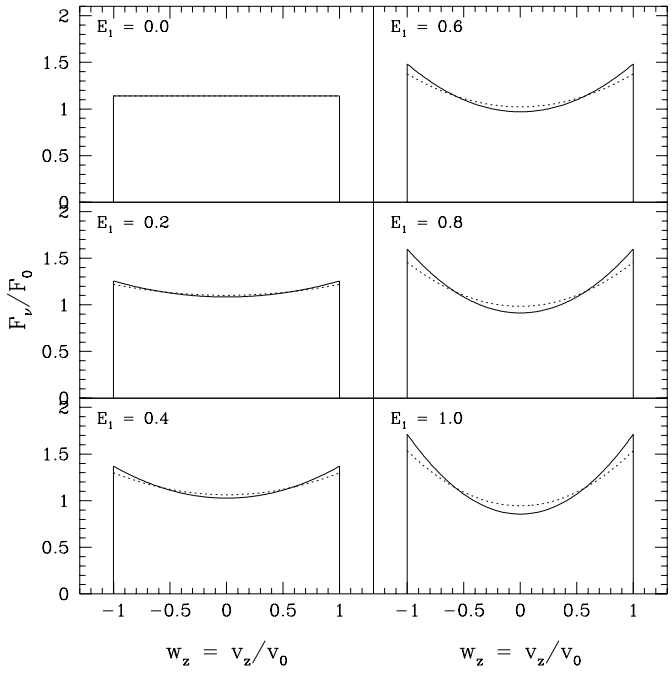

Fig. 4. Line profiles showing the effects of finite star depolarization (dotted)

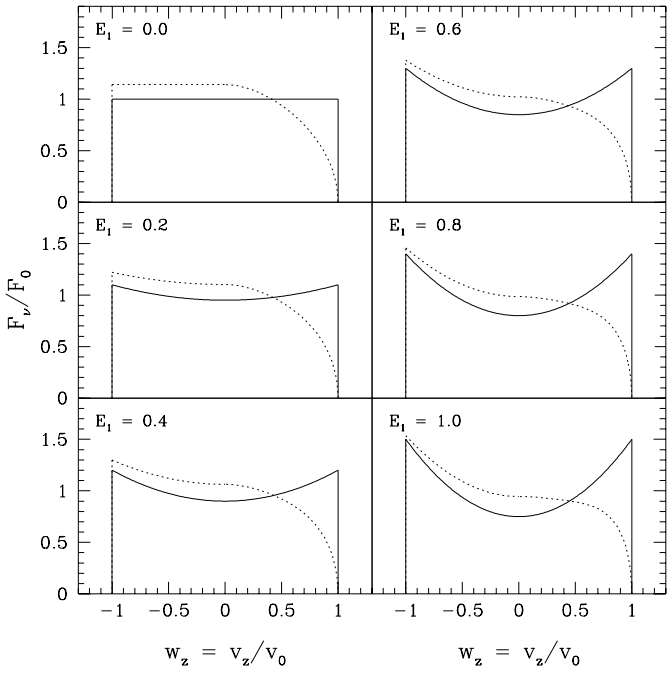

Fig. 5. Resonance scattering line profiles for a spherical wind and six values of the E_1 parameter including both stellar occultation and finite star depolarization (shown as dotted)

with finite star depolarization, a reduction of about 30% which is consistent with the results of Cassinelli et al. (1987; see Fig. 6 of their paper).

A second difference is the leading factor of $(\pi - 2) = 1.14$. This new coefficient scales up the overall line emission. Its appearance reflects the fact that for a finite star, more light is available for scattering at a fixed point in the extended envelope than is the case for just point star illumination. This result can be understood from the following example. Consider a scatterer located just above the photospheric stellar surface at radius R_*. This hypothetical scatterer experiences an incident radiation field of magnitude $W(R_*)I_\nu^* = L_\nu/8\pi^2 R_*^2$, where $W(r)$ is the familiar dilution factor. In the case of a point star, a scatterer located at R_* (taken as the inner boundary of the scattering medium) experiences a radiation field that is only half as large, $L_\nu/16\pi^2 R_*^2$. The dilution factor tends toward the inverse square law form appropriate for a point star only as $r \gg R_*$.

Having derived expressions for the emission line profile that consider individually the consequences of stellar occultation and finite star depolarization, these effects are combined in the next section.

2.1.4. The complete finite star case

The profile shapes resulting from considerations of both occultation and finite star depolarization can be derived by using Eq. (3) that includes the Eddington moments J_ν and K_ν and by integrating over the scattering volume that excludes the emission which is occulted by the star. Although more complicated than previous expressions, the integral solution is analytic for the case of constant expansion (see App. A), and in the optically thin limit, the solution for the *redshifted* emission is given by

$$\frac{F_\nu(w_z)}{F_0} =$$

$$\left\{ \left[\pi - 2\sin^{-1} w_z - 2\sqrt{\frac{1-w_z}{1+w_z}} \right] - \frac{1}{8} E_1 \left(1 - 3{w_z}^2\right) \right.$$

$$\left. \left(w_z \sqrt{1-{w_z}^2} + \sin^{-1}\sqrt{1-{w_z}^2} \right) \right\}. \qquad (10)$$

For the blueshifted emission, the line profile is given by Eq. (9), because there is no stellar occultation for the blueshifted component.

From Fig. 5, it is clear that stellar occultation is the dominant effect in altering the profiles from the overall double-horned shapes that were derived in the point star case. Even so, as previously noted, the effect of occultation is to produce a "bubble" shaped emission profile in the red wing, and the consequence of the anisotropic scattering is to recover a more nearly flat-top profile. Comparing the cases of isotropic scattering $E_1 = 0$ with dipole scattering $E_1 = 1$, the HWHM in the red wing is about 12% broader for dipole scattering. In addition, the central emission of the dipole scattering case is depressed by 17% relative to the isotropic scattering result. When a more realistic wind velocity distribution is added, as done in the following section, anisotropic scattering alone is expected to significantly alter the profile appearance, but the stellar occultation greatly reduces the consequences of the anisotropy. Nonetheless, the general

trends of central depression in the line emission and broadening of the line persist.

2.2. Resonance line profiles from spherical winds with velocity stratification

Having acquired some intuition about the anisotropic scattering effects from the simplified examples of the previous sections, the discussion now turns toward line profiles arising from more realistic stellar wind models. The computation of resonance line scattering profiles is accomplished by employing the Sobolev-P method of Jeffery (1988). Hence, a brief description of Sobolev-P is given first, followed by an example set of profile calculations as a function of line optical depth in a wind with a velocity stratification.

2.2.1. The Sobolev-P method

The Sobolev-P formalism for approximating radiative transfer in moving media was developed by Jeffery (1988) and generalized to applications in 3-dimensions in Jeffery (1990). The method is based on the well-known Sobolev approximation for envelopes with large velocity gradients and extended to the case of resonance line scattering polarization. Although the Sobolev approximation is known to be inferior to the more rigorous comoving frame radiative transfer calculation, yet some aspects of the Sobolev method are reasonably accurate, such as the identification of isovelocity zones as seen by the observer (Hamann 1981), and of course the approximation yields a major simplication to the computation of the radiative transfer (e.g., see Lamers et al. 1987). Given the computational advantages of the Sobolev approximation combined with the exploratory nature of this paper, the Sobolev-P method has been adopted to demonstrate, at least qualitatively if not quantitatively, the consequences of anisotropic line scattering for observed profiles from spherical winds.

For the implementation of the Sobolev-P method, the reader is referred to Jeffery (1990). The case of spherical symmetry offers an enormous simplification for the numerical calculations. Here the line profiles are computed assuming that collisional de-excitations are negligible compared to spontaneous decay. In Jeffery's notation this implies that $\epsilon = 0$, and as there is no source of nonscattering line photons, Jeffery's Stokes parameter $\mathbf{G}$ is also zero. Lastly for a fixed wind velocity law, the different profiles are distinguished by the optical depth constant, τ_0, where the Sobolev line optical depth at any point in the wind is given by

$$\tau_\nu = \frac{k_l}{\lambda_l}\left|\frac{\mathrm{d}v}{\mathrm{d}s}\right|^{-1} \equiv \tau_0\, x^{-1}\, w^{-2}\,(1+\mu^2\,\sigma)^{-1}, \qquad (11)$$

with k_l the integrated line opacity coefficient, λ_l the wavelength of the line, $x = r/R_*$, $w = v_\mathrm{r}/v_\infty$, $\mu = \cos\vartheta$, and $\sigma = \mathrm{d}\ln w/\mathrm{d}\ln x - 1$. Eq. (11) is appropriate for a resonance line with an opacity proportional to the wind density. Implicit in the parametrization of the line optical depth is the assumption of constant ionization. A radially varying ionization distribution is easy to include, but such a distribution presents an additional free parameter that (a) is somewhat arbitrary for this exploratory work and (b) has little influence on the conclusions that will be presented. It is worthwhile noting that in the optically thin limit, the Sobolev-P results analytically reduce to those derived in the previous sections.

2.2.2. Line profile results

An exhaustive consideration of the line profiles that would result for different wind velocity distributions would be prohibitively long, so a single illustrative example is presented. A standard β-law form of the velocity law is chosen, with $v_\mathrm{r} = v_\infty(1 - R_0/r)^\beta$. A value of $\beta = 1$, consistent with theoretical predictions (Friend & Castor 1983) and observational inferences of many hot star winds (e.g., Bertout et al. 1985), is taken for the profile calculations presented below.

The wind density distribution now becomes $n(r) = R_*^2 v_\infty / r^2 v_\mathrm{r}$. To avoid a singular value of the wind density profile at the lower radius R_*, the parameter R_0 is chosen to be $R_0 = 0.95R_*$. Line profiles for $\tau_0 = 0.3$, 1.0, 3.0, and 10.0 are displayed in Fig. 6. The solid line is for the case of pure isotropic scattering ($E_1 = 0$) and the dashed for pure dipole scattering ($E_1 = 1$). Also displayed in the lower right of each panel is the percentage difference in line emission between the two profiles, with the line emission being measured *from* the continuum level. In all four cases, it is the emission of the dipole scattering that is centrally depressed, which occurs because near line center the emission arises predominantly from the Sobolev zones where stellar photons must scatter through large angles of about $90°$. For light that is Rayleigh scattered through nearly right angles, the emergent intensity is smaller than that which is forward or backward scattered. In the optically thin lines, the difference in emission peaks is slightly greater than 10%. Even for $\tau_0 = 3.0$, the peak emission of the two cases differs by just under 10%. Only at large optical depths do the isotropic and dipole scattering profiles become nearly indistinguishable. As the line optical depth approaches large values, the Stokes source function tend toward isotropic scattering, as expected since the line photons must multiply scatter to escape the isovelocity zone.

In addition to differences in peak emission, the isotropic and dipole scattering profiles also differ in their broadening. Relative to the case of isotropic scattering, the dipole scattering lines show enhanced emission in the wings. Again, this can be explained in terms of the Rayleigh scattering, in which the brighter forward and backward scattered light corresponds to isovelocity zones located at Doppler shifts toward that of the wind terminal speed. The differences in HWHM of the redshifted emission are only slight, at the 10% level.

The fact that the dipole scattering emission is centrally depressed but slightly broadened results in the total line equivalent width being similar to that of the isotropic scattering case, with variations at the 5% level. Note that any contribution made by photospheric absorption has also been ignored, but emphasis is here given to just the anisotropic scattering in the wind. The

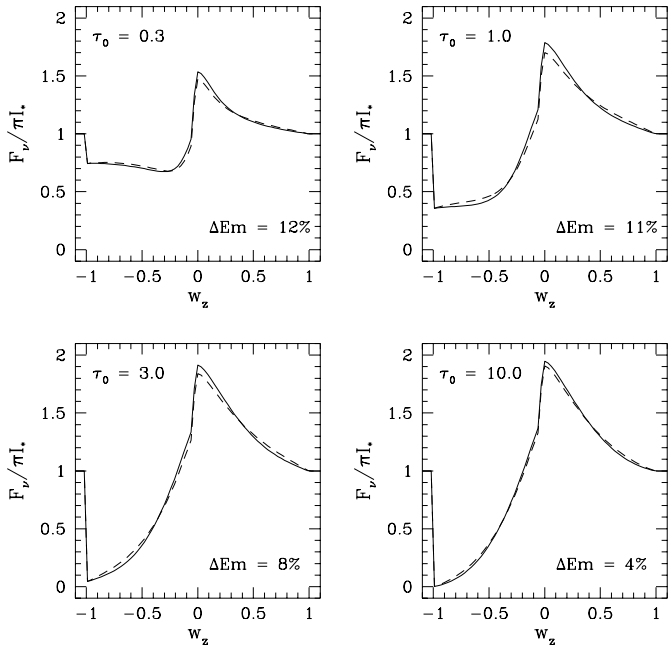

Fig. 6. Four line profiles of differing optical depths (as labeled) using the Sobolev-P method. The solid is for isotropic ($E_1 = 0$) scattering whereas the dashed is for dipole ($E_1 = 1$) scattering. The percentages indicate the difference in the line emission (i.e., for the continuum subtracted line profile) of the two cases as measured at line center.

presence of photospheric absorption will mostly modify the line profile near line center, which will likely obscure the effects of the anisotropic scattering for the central emission. The observational consequences of the results presented in this section are examined next.

3. Discussion

The effects of anisotropic scattering for resonance line profiles formed in spherical winds have been investigated. It is concluded that the combined occurrences of stellar occultation and finite star depolarization severely limit the modification of the wind line profiles that would otherwise be present in resonance lines that have a strong dipolar contribution to their scattering. In the best cases, only mild differences at the 10% level appear between lines arising from pure isotropic scattering and those from pure dipole scattering, with the latter case producing profiles that are slightly depressed in central emission and somewhat broadened in the HWHM of the red wing. These results were obtained using a Sobolev approximation, which is known to disagree somewhat with more sophisticated co-moving line formation calculations. However, the fairly small modification of the line profile by the dipole scattering is not likely to change much with a more accurate treatment of the radiative transfer. The neglect of both a photospheric absorption component and the consequences of collisional de-excitation for the line emission suggest that even the 10% level difference derived here between the two extreme cases of isotropic and dipole scattering appears at best generous.

The conclusion that anisotropic scattering has little, even negligible, effect on resonance line profiles in spherical winds is rather important for two reasons. (1) Several tables are found in App. A of Jeffery (1989) that are useful for computing E_1 values different line transitions. For example, values of E_1 for several strong resonance lines (and a few of the Balmer lines) found at ultraviolet and visible wavelengths are listed in Table 1. In particular, several of the most important resonance lines used in the analysis of hot stellar winds are doublets, such as N V 1239, Si IV 1394, and C IV 1550. All three of these doublets arise from Lithium like atoms with transitions of the type $^2S_{1/2}-^2P_{1/2,3/2}$. It is seen from Table 1 that the short wavelength component in each case has a value of $E_1 = 0.5$, but the long wavelength component has $E_1 = 0$. Even though the E_1 values for the two doublet components are quite different, the results of Sect. 2.2 suggest that analyses of these important lines based on the usual assumption of isotropic scattering are probably adequate.

(2) A typical line profile fit analysis for hot stellar winds proceeds roughly as follows (e.g., Bjorkman et al. 1994): make assumptions about the wind geometry and possibly the wind velocity distribution (based on a theory), then fit one or several P Cygni lines by adjusting the mass loss rate, turbulent broadening, and wind ionization distribution. In particular, the ionization distribution of the atoms is not well understood (Groenewegen & Lamers 1991; MacFarlane et al. 1994). Thus, if anisotropic scattering were to have a significant influence on the resonance line profile shape, it would be difficult to distinguish that influence from ambiguities associated with the ionization structure (and also the wind velocity distribution if a free parameter in the fit procedure). Given the common assumption of isotropic scattering and assuming that anisotropic scattering is affecting the line emission being studied, a typical profile fitting algorithm will force the ionization distribution to vary in such a way as to account for the anisotropic effects. It is therefore comforting to find that resonance lines formed in spherical winds are little affected by anisotropic scattering, at least to $\lesssim 10\%$.

The only case where the dipole component to the resonance scattering has significant effects in spherical winds is that of a shell of large radius, for which the star is nearly a point source and the wind expands at a constant speed so that the results of Fig. 2 and Sect. 2.1.1 apply. Such a scenario may be rare but might arise for example in the following situations. (a) The ionization structure of atomic species are known to be radially stratified in the winds of the Wolf-Rayet stars, with highly ionized species (e.g., N V, O VI, C IV) occurring at the innermost radii and lower ionized species (e.g., He I, N IV, O III, C III) occurring only at larger radii (Schulte-Ladbeck et al. 1995). It is the formation of resonance lines from atoms of low ionization located at large radii for which anisotropic line scattering may more significantly modify the profile shape. (b) Resonance line scattering in a shell of large radius may arise not as a steady phenomenon of which the Wolf-Rayet winds are an example, but as a transient phenomenon that might occur as a result of a nova or supernova explosion. In this latter case, resonance lines arise from the scattering of the intense radiation field of the central explosion as the flux propagates through an extended and

Table 1. The E_1 Values of some common resonance lines

Ion	Transition	λ (Å)	E_1
O VI	$2\,^2S_{1/2} - 2\,^2P_{3/2}$	1031.9	0.5
	$2\,^2S_{1/2} - 2\,^2P_{1/2}$	1037.6	0.0
P V	$3\,^2S_{1/2} - 3\,^2P_{3/2}$	1118.0	0.5
	$3\,^2S_{1/2} - 3\,^2P_{1/2}$	1128.0	0.0
Si III	$3\,^1S_0 - 3^1\,P_1$	1206.5	1.0
N V	$2\,^2S_{1/2} - 2\,^2P_{3/2}$	1238.8	0.5
	$2\,^2S_{1/2} - 2\,^2P_{1/2}$	1242.8	0.0
Si IV	$3\,^2S_{1/2} - 3\,^2P_{3/2}$	1393.8	0.5
	$3\,^2S_{1/2} - 3\,^2P_{1/2}$	1402.8	0.0
C IV	$2\,^2S_{1/2} - 2\,^2P_{3/2}$	1548.2	0.5
	$2\,^2S_{1/2} - 2\,^2P_{1/2}$	1550.8	0.0
Mg II	$3\,^2S_{1/2} - 3\,^2P_{3/2}$	2796.4	0.5
	$3\,^2S_{1/2} - 3\,^2P_{1/2}$	2803.5	0.0
Ca II	$4\,^2S_{1/2} - 4\,^2P_{3/2}$	3934.8	0.5
	$4\,^2S_{1/2} - 4\,^2P_{1/2}$	3969.6	0.0
Ca I	$4\,^1S_0 - 4\,^1P_1$	4227.9	1.0
Hγ		4339.4	0.34[a]
Hβ		4860.1	0.34[a]
Na I	$3\,^2S_{1/2} - 3\,^2P_{3/2}$	5891.6	0.5
	$3\,^2S_{1/2} - 3\,^2P_{1/2}$	5897.6	0.0
Hα		6561.1	0.35[a]
K I	$4\,^2S_{1/2} - 4\,^2P_{3/2}$	7667.0	0.5
	$4\,^2S_{1/2} - 4\,^2P_{1/2}$	7701.0	0.0

[a] Values taken from Jeffery (1989)

pre-existing circumstellar envelope. Although not an example of spherical symmetry, a similar circumstance appears to have occurred for the N V 1239 resonance line from the equatorial ring surrounding SN1987A (Lundqvist & Fransson 1996).

If resonance lines should form from scattering in an optically thin shell of large radius and constant expansion, however such a circumstance may arise, Eq. (7) provides a simple testable prediction about the resulting line profile structures. If multiple resonance lines are observed that sample a range of E_1 values, the profiles will also exhibit a range of shapes, with differing wing to line center emission ratios. An analytic expression for the wing to center emission contrast as derived from Eq. (4) is

$$\frac{F_\nu(w_z = \pm 1)}{F_\nu(w_z = 0)} = 2\left(\frac{2 + E_1}{4 - E_1}\right), \qquad (12)$$

with contrast values from 1 at $E_1 = 0$ to 2 at $E_1 = 1$. Clearly, if a double-horned profile shape persists for all observed resonance lines independent of the E_1 value, the wind is likely not spherical–at least not spherical and smooth (e.g., the wind could be asymmetrically clumpy but spherical in the time average).

Throughout this paper discussion has centered on the anisotropic scattering in spherical winds. But the anisotropic resonance line scattering may have interesting observational consequences for other types of wind geometries. One particular example is that of rotating and/or expanding equatorial disks, which tend to produce double-horned emission profiles (Lamers & Cassinelli 1997). It can be shown that the line profile shape from a geometrically and optically thin equatorial ring of constant expansion is indistinguishable from a profile arising in a ring of constant rotation, if the resonance line scattering is isotropic and there is neither occultation nor absorption. However, for nonzero values of the E_1 parameter, the dipole contribution to the scattering makes the profiles from expanding rings distinct from those of rotating rings and affords the opportunity to observationally discriminate between the two. A separate paper to explore the possibility of diagnosing expansion and rotation using resonance line scattering profiles from equatorial disks is planned.

Yet another regime where the consequences of resonance line scattering discussed in this paper may produce significant and observable effects in the line profile shapes is that of line formation in relativistically moving media. For example, Hutsemékers (1990) has investigated the formation of P Cygni lines in relativistically expanding and spherical atmospheres under the assumption of isotropic scattering. The relativistic motions produce significant distortions of the isovelocity zones, in both shape and interval spacing. In contrast to the nonrelativistic case considered here, the anisotropic line scattering may play a more prominent role in the profile shape for winds expanding at near the speed of light. Alternatively, if a compact object (e.g., a black hole) were embedded in the scattering medium, even if that medium were not moving at relativistic speeds, the photon trajectories of the scattered photons can deviate significantly from straight lines if passing close to the central compact object. For example, Bao et al. (1994) calculated line profiles formed in accretion disks surrounding a black hole. In their simulations photons that would not be normally observed (e.g., light emitted from the backside of the disk relative to the observer's position) can contribute significantly to the line emission owing to the curved paths of the photons. The dipole scattering contribution could have relevance for the predicted profiles shapes of such a scenario. Extending these ideas to spherical symmetry, it is clear that the occultation, which so dramatically reduces the consequences of anisotropic line scattering in the nonrelativistic cases presented here, may be circumvented in the presence of a central compact object owing to the effect of gravitational lensing. However, these topics are beyond the scope of this paper and are directions for future investigation.

Acknowledgements. The author wishes to express gratitude to Profs. J. C. Brown, J. P. Cassinelli, D. Clarke, and K. H. Nordsieck for helpful

discussions and for encouragement in pursuing the topic of this paper. Thanks also to Dr. M. Hendry for proofreading the manuscript. This research was conducted under funding from a UK PPARC Rolling Grant.

Appendix A: Optically thin resonance line scattering with stellar occultation and finite star depolarizaton

The object of this appendix is to derive Eq. (10) for the analytic expression of the wind emission line profile arising from resonance scattering in an optically thin line and that includes the effects of both stellar occultation and finite star depolarization. Since stellar occultation affects only the redshifted part of the line profile, the blueshifted emission (i.e., not accounting for the wind absorption) is given by Eq. (9) that accounts for the finite depolarization.

To solve for the emission of the redshifted wing, consider Eq. (3) for the flux of resonant scattered light by the wind at a given frequency in the profile. Substituting the well-known expressions for the Eddington moments J_ν and K_ν, the integration over the isovelocity zone becomes

$$\frac{F_\nu(v_z)}{F_0} = 2\int_{r(v_z)}^{\infty}\left[(1-\cos\vartheta_*) - \frac{1}{8}E_1\,(1-3\cos^2\vartheta)\cos\vartheta_*(1-\cos^2\vartheta_*)\right]\frac{dr}{R_*}, \quad \text{(A1)}$$

where $\cos\vartheta_* = \sqrt{1-R_*^2/r^2}$ and $\cos\vartheta = -v_z/v_0$ for constant expansion v_0. The presence of the geometrical factor $\cos\vartheta_*$ insures that the finite depolarization is taken into account. The stellar occultation enters the integral through the lower limit $r(v_z)$, which is determined by the intersection of a given isovelocity zone with the cylindrical occulting tube lying behind the star and opposite the observer's viewing line-of-sight. The lower limit is given by $r(v_z) = R_*/\sqrt{1-v_z^2/v_0^2}$.

The integrand of (A1) is composed of two terms which shall be treated separately and then combined to obtain the full solution for the redshifted profile emission. The first term is

$$I_1 = 2\int_{r(v_z)}^{\infty}(1-\cos\vartheta_*)\,\frac{dr}{R_*} = 2\int\left(1-\sqrt{1-\frac{R_*^2}{r^2}}\right)\frac{dr}{R_*}. \quad \text{(A2)}$$

The integral for I_1 has solution

$$I_1 = \pi - 2\left(\frac{1-\sqrt{1-\frac{R_*^2}{r^2(v_z)}}}{1+\sqrt{1-\frac{R_*^2}{r^2(v_z)}}}\right)^2 - 2\sin^{-1}\sqrt{1-\frac{R_*^2}{r^2(v_z)}}. \quad \text{(A3)}$$

Substituting for $r(v_z)$ and adopting a change of variable $w_z = v_z/v_0$ yields

$$I_1 = \pi - 2\sqrt{\frac{1-w_z}{1+w_z}} - 2\sin^{-1}w_z. \quad \text{(A4)}$$

The second term is

$$I_2 = \frac{1}{4}E_1\,(1-3\cos^2\vartheta)\int_{r(v_z)}^{\infty}\cos\vartheta_*\,(1-\cos\vartheta_*^2)\,\frac{dr}{R_*} = \frac{1}{4}E_1\,(1-3\cos^2\vartheta)\int_{r(v_z)}^{\infty}\sqrt{1-\frac{R_*^2}{r^2}}\left(\frac{R_*^2}{r^2}\right)\frac{dr}{R_*}. \quad \text{(A5)}$$

The solution to the integral for I_2 is

$$I_2 = \frac{1}{8}E_1\,(1-3\cos^2\vartheta)\left[\frac{R_*}{r(v_z)}\sqrt{1-\frac{R_*^2}{r^2(v_z)}} + \sin^{-1}\frac{R_*}{r(v_z)}\right]. \quad \text{(A6)}$$

Substituting for $r(v_z)$ and using $w_z = v_z/v_0$ gives

$$I_2 = \frac{1}{8}E_1\,\left(1-3w_z^2\right)\left(w_z\sqrt{1-w_z^2} + \sin^{-1}\sqrt{1-w_z^2}\right). \quad \text{(A7)}$$

The complete solution to Eq. (A1) is just the difference $I_1 - I_2$, which by inspection of Eqs. (A4) and (A7) gives the result of Eq. (10).

References

Bao, G., Hadrava, P., Østgaard, E., 1994, ApJ 435, 55
Bertout, C., Leitherer, C., Stahl, O., Wolf, B., 1985, A&A 144, 87
Bjorkman, J. E., Ignace, R., Tripp, T. M., Cassinelli, J. P., 1994, ApJ 435, 416
Caroff, L. J., Noerdlinger, P. D., Scargle, J. D., 1972, ApJ 176, 439
Cassinelli, J. P., Nordsieck, K. H., Murison, M. A., 1987, ApJ 290, 302
Chandrasekhar, S., 1960, Radiative Transfer (New York: Dover)
Friend, D. B., Abbott, D. C., 1986, ApJ 311, 701
Friend, D. B., Castor, J. I., 1983, ApJ 272, 259
Groenewegen, M. A. T., Lamers, H. J. G. L. M., 1991, A&A 243, 429
Hamann, W.-R., 1981, A&A 93, 353
Hamilton, D. R., 1947, ApJ 106, 457
Hutsemékers, D., 1990, ApJ 361, 367
Jeffery, D. J., 1988, Ph.D. Thesis, McMaster University
Jeffery, D. J., 1989, ApJS 71, 951
Jeffery, D. J., 1990, ApJ 352, 267
Kudritzki, R. P. Hummer, D. G., 1990, ARAA 28, 303
Lamers, H. J. G. L. M., Cerruti-Sola, M., Perinotto, M., 1987, ApJ 314, 726
Lamers, H. J. G. L. M., Cassinelli, J. P., 1997, Introduction to Stellar Winds, in press
Lundqvist, P., Fransson, C., 1996, ApJ 464, 924
MacFarlane, J. J., Cohen, D. H., Wang, P., 1994, ApJ 437, 351
McKenna, S. J., 1984, Ap&SS 106, 283
McKenna, S. J., 1985, Ap&SS 108, 31
Mihalas, D., 1978, Stellar Atmospheres (Freeman: New York)
Nagendra, K. N., 1988, ApJ 335, 269
Pauldrach, A., Puls, J., Kudritzki, R. P., 1986, A&A 164, 86
Schulte-Ladbeck, R. E., Eenens, P. R. J., Davis, K., 1995, ApJ 454, 917
Stenflo, J. O., 1994, Solar Magnetic Fields (Dordrecht: Kluwer)
Struve, O., 1931, ApJ 73, 94